Distinguishing optical rectification, four-wave mixing, and surface depletion effects in coherent control of terahertz generation in ZnSe under normal and oblique incidence

Xueqin Cao, Leidong Xing, Fan Wang, Xukun Feng, Yuanyuan Huang,* and Xinlong Xu†

Shaanxi Joint Lab of Graphene, State Key Lab Incubation Base of Photoelectric Technology and Functional Materials, International Collaborative Center on Photoelectric Technology and Nano Functional Materials, Institute of Photonics & Photon-Technology, Northwest University, Xi'an 710069, People's Republic of China

(Received 8 April 2024; revised 28 July 2024; accepted 19 August 2024; published 4 September 2024)

Coherent control under two-color femtosecond laser excitation plays a significant role in atomic, molecular, and semiconductor materials. Recently, terahertz (THz) emission spectroscopy has been employed to characterize the coherent ultrafast photocurrent from semiconductor materials under two-color light excitation. However, distinguishing the contributions of various optical effects to THz radiation under normal- and oblique-incident excitations with two-color light remains a challenge. Herein, we choose the zinc selenide (ZnSe) crystal as a model sample to study the THz radiation at normal and oblique incidences with two-color light excitation. Based on the dependence of the THz signal on the relative phase difference between the fundamental wave (800 nm, ω) and the second harmonic wave (400 nm, 2ω), the contribution ratio of optical rectification (OR) to four-wave mixing (FWM) for THz radiation is calculated as 1:2.3 at normal incidence. Under oblique incidence, the contribution ratios of FWM, OR, and surface depletion field (SDF) for THz radiation are calculated as 1:1.5:6.7. In particular, we have observed the THz time-domain signals from net FWM contribution with polarity reversal at both normal and oblique incidences. This work not only elucidates the THz radiation properties of ZnSe crystal but also reveals the interplay among OR, SDF, and FWM in the coherent control of ultrafast photocurrent under femtosecond laser excitations.

DOI: 10.1103/PhysRevB.110.125302

I. INTRODUCTION

Coherently controlled photocurrent is essential for advancing research in the fields of atomic [1], molecular [2], and semiconductor materials [3]. Compared to atoms and molecules, semiconductor materials have sparked interest due to their ability to enable coherent control in momentum space over the amplitude and direction of photocurrents [4,5]. Recently, terahertz (THz) emission spectroscopy has been employed to characterize the coherent ultrafast photocurrent from semiconductor materials under two-color light excitation [6–11], as THz emission spectroscopy technique can reveal multiple physical information such as amplitude, polarity, and phase. Previously, even though the coherent control of THz radiation has been investigated in some semiconductors, including silicon [12], GaAs [13], graphene [14], Bi_2Se_3 [15], and Bi_2S_3 [7], only the single four-wave mixing (FWM) mechanism is revealed for the THz radiation under normal-incident excitations in most reported works, which are far from the practically applied scenarios. In fact, optical effects induced by a single-color excitation, such as optical rectification (OR) effect [16], photogalvanic effect [17], and surface depletion field (SDF) effect [18], can also inevitably participate in the process of THz radiation from semiconductors under the two-color light excitation. The presence of these effects significantly impacts the elaboration of the FWM effect and measurements of coherently controlled THz radiation. It is a complicated yet interesting issue of how to distinguish the multiple optical effects simultaneously contributing to the THz radiation, and realize the quantum interference in semiconductors at both normal- and oblique-incident excitations.

Herein, zinc selenide (ZnSe) crystal as a model semiconductor is used to understand the THz radiation at normal and oblique incidences with two-color light excitation. The isotropic response (two fold rotational symmetry) with respect to the azimuthal angle under single 400-nm (800-nm) laser excitation is attributed to the SDF (OR) effect. Under the two-color laser excitation, the THz peak-valley amplitude with the pump fluence exhibits a high-order dependence under normal incidence, while it exhibits a saturation dependence under oblique incidence. These results indicate that the FWM dominates THz generation of ZnSe under normal incidence, while the SDF dominates THz generation of ZnSe under oblique incidence. Most importantly, we have extracted the net contribution of FWM to THz radiation and observed that the THz time-domain signal exhibited the polarity reversal at the relative phase differences of $\pi/2$ and $3\pi/2$. This work not only examines the THz radiation of ZnSe under individual fundamental (ω) and second harmonic (2ω) light excitations but also provides an effective method to distinguish multiple optical effects under both normal and oblique incidences with the two-color excitation for clear quantum interference observation.

*Contact author: yyhuang@nwu.edu.cn
†Contact author: xlxuphy@nwu.edu.cn

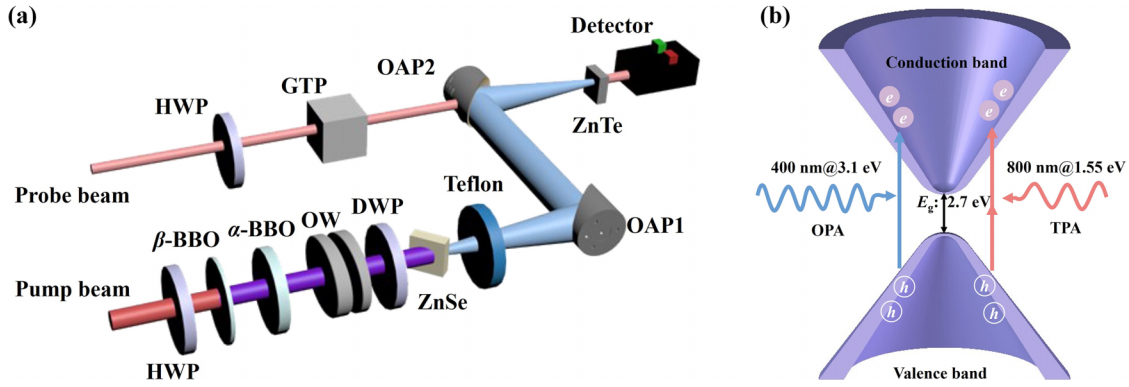

FIG. 1. (a) Experimental setup for coherent control of THz generation under two-color (400+800-nm) excitation. HWP: half wave plate. OW: optical wedges. DWP: dual-wave plate. OAP: off-axis parabolic. GTP: Glan-Taylor prism. (b) Microscopic physics of coherently controlled photocurrent in ZnSe crystal. OPA: one-photon absorption. TPA: two-photon absorption.

II. RESULTS AND DISCUSSIONS

Figure 1(a) displays the experimental setup for coherent control of THz generation under two-color (400+800-nm) excitation. A Ti:sapphire regenerative amplifier (Spitfire Ace, Spectra-Physics) generates 800-nm laser pulses with a pulse duration of 35 fs and a repetition rate of 1 kHz. After passing through the beam splitter, the laser beam is split into the probe beam and the pump beam. A half wave plate (HWP) and a Glan-Taylor prism (GTP) are used to adjust the intensity of the probe beam. Another HWP is used to change the polarization angle of the pump beam. The pump beam (800 nm, ω) passes through a β-BBO (BaB_2O_4) crystal to generate the frequency doubling wave (400 nm, 2ω), while a α-BBO is used to compensate the positive dispersion. The full width at half maxima of 800- and 400-nm pulses are 0.976 and 0.568 mm, respectively, at the focused position. The thicknesses of the β-BBO and α-BBO crystals are 0.2 and 7.5 mm, respectively. For the β-BBO crystal, the horizontal overlap length of the ω and 2ω can be described as: $L_a = a/\tan\theta$, where a is the diameter of the ω light; θ is the walk-off angle that is given by $\tan\theta = \frac{1}{2}(n_o^{\omega})^2[(n_o^{2\omega})^{-2} - (n_e^{2\omega})^{-2}]\sin(2\theta_m) = 0.056$ [19]. The refraction index n_o^{ω}, $n_o^{2\omega}$, and $n_e^{2\omega}$ are obtained from $n_o^2 = 2.7359 + \frac{0.01878}{\lambda^2 - 0.01822} - 0.01354\lambda^2$ and $n_e^2 = 2.3753 + \frac{0.01224}{\lambda^2 - 0.01667} - 0.01516\lambda^2$ [20]. The θ_m (29.2°) is the angle between the ω light and the optical axis. The calculated horizontal overlap length (17.43 mm) is much larger than the thickness of the β-BBO crystal. Hence, the walk-off effect can be ignored. The relative phase between the fundamental (ω) and harmonic (2ω) waves is controlled by the optical wedges (OW). We experimentally determined the temporal overlap of the ω and 2ω pulses in time-domain by comparing the peak positions of the THz time-domain signals, and we theoretically calculated the dispersion caused by every optical component inserted in the optical path of ω pulse and 2ω pulse. When inserting the optical wedges with a thickness of 6.9 mm, the resultant positive dispersion is precisely counteracted by the negative dispersion provided by the α-BBO crystal, of which the thickness was optimized to achieve perfect compensation. We use a collinear two-color excitation configuration in the THz emission experiment. As such, after passing through the β-BBO crystal, the 2ω propagates collinearly with the ω. The dual-wave plate (DWP) is used to adjust the relative polarization between the fundamental and the second harmonic waves. The pump laser is blocked after passing through a Teflon plate. After passing through a pair of off-axis parabolic (OAP) mirrors, the generated THz waves are focused onto the detection crystal (⟨110⟩ ZnTe) while the probe beam is also focused collinearly with the THz waves onto the ZnTe crystal. Finally, the generated THz waves are detected using the electro-optic sampling method [17]. The single-color pump setup is depicted in Appendix A.

Figure 1(b) depicts the microscopic physics of coherently controlled photocurrent in the ZnSe crystal (with Raman spectrum shown in Fig. 7 in Appendix B). Since the bandgap of ZnSe is 2.7 eV [21,22], the photon energy of 400-nm (3.1 eV) excitation is above the bandgap and results in one-photon absorption [6], while the 800-nm (1.55 eV) excitation with the photon energy below the bandgap leads to two-photon absorption [23]. These two processes can result in the quantum interference in the momentum space and further coherently control the THz radiation by the relative phase between the ω and 2ω pulses [7]. However, the observation of quantum interference in solid state is nontrivial as many other photophysics processes such as OR and SDF in semiconductors can also contribute to the THz generation, which veil the process of quantum coherence.

Figure 2(a) shows the simplified diagram of the THz emission in a transmission configuration, where ψ is the polarization angle of the pump beam, θ is the incident angle, γ is the azimuthal angle of the sample. XYZ and $X'Y'Z'$ are the laboratory coordinate and crystalline coordinate systems, respectively. In order to unveil the process of quantum coherence by THz emission spectroscopy, we first design the THz generation experiments under single 800- and 400-nm excitations. At the fixed pump fluences of 0.127 mJ/cm^2 (800 nm) and 0.014 mJ/cm^2 (400 nm), Figs. 2(b) and 2(c) present the THz peak-valley amplitude signals as a function of the azimuthal angle of ZnSe crystal under single 800- and 400-nm excitations, respectively, with red dots/circles standing for 0° incidence and blue dots/circles for 40° incidence. The red/blue dots with positive values represent the THz valley-peak-valley waveforms, while the red/blue circles with negative values represent the THz peak-valley-peak waveforms. It is evident that the THz signal under 40° incident angle (blue) is quite larger than that under 0° incident angle (red), which is

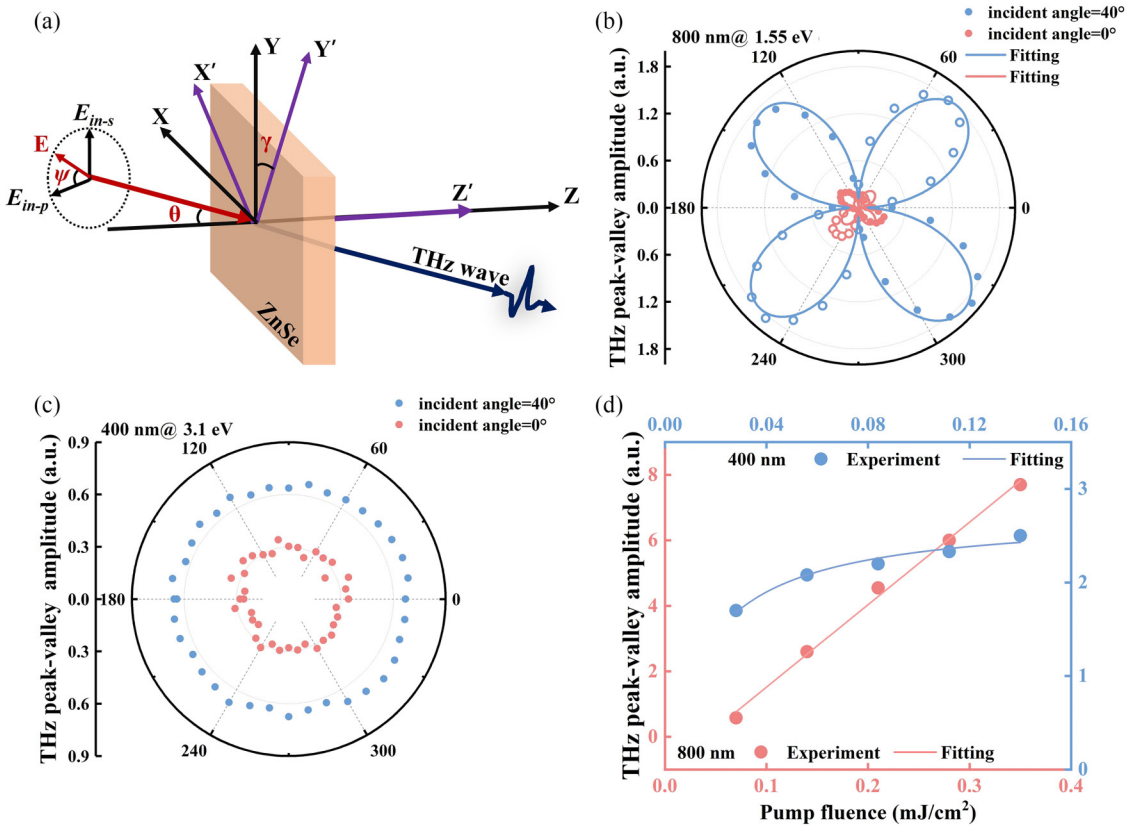

FIG. 2. (a) Simplified diagram of THz generation in a transmission configuration, where ψ is the polarization angle of the pump beam, θ is the incident angle, γ is the azimuthal angle of the sample. XYZ and $X'Y'Z'$ are the laboratory coordinate and crystalline coordinate systems, respectively. THz peak-valley amplitude with respect to the azimuthal angle of ZnSe crystal under (b) single 800-nm and (c) single 400-nm excitations at 0° (red) and 40° (blue) incident angles. The red/blue dots with positive values represent the THz valley-peak-valley waveforms, while the red/blue circles with negative values represent the THz peak-valley-peak waveforms. The solid lines are fitting results. (d) Pump fluence dependence of the THz peak-valley amplitude under the single 800-nm (red) and 400-nm (blue) excitations. The solid lines are fitting results.

already magnified by a factor of 4 for clarity under normal incidence in Figs. 2(b) and 2(c). As a comparison, the azimuthal angle dependence of THz signal demonstrates an obvious twofold rotational symmetry under the 800-nm excitation, while that under the 400-nm excitation exhibits isotropic response. This difference can be observed at both 0° and 40° incidences, which suggests the different THz generation mechanism under different wavelength excitations. Usually, the azimuthal angle dependence of THz signal below the bandgap excitation demonstrates nonlinear optical response determined by the crystal symmetry of semiconductors. For example, the MoS_2 [16] and SnS_2 [24] display a threefold rotational symmetry on the azimuthal angle as they belong to 3m point group, which are attributed to the second-order nonlinear optical response (so-called OR). According to the $\bar{4}3m$ point group of ZnSe, the THz peak-valley amplitude based on the OR model is described as (details in Appendix D):

$$E_{\mathrm{THz}} \propto A \sin 2\gamma + B \sin(\gamma + \pi/4) + C, \tag{1}$$

where the γ represents the azimuthal angle of ZnSe as shown in Fig. 2(a). The constants A and B are related to the nonlinear susceptibility, while the constant C is independent on the nonlinear susceptibility. The theoretical results are in good agreement with the experimental results as shown in Fig. 2(b). Hence, the dominant THz radiation of ZnSe is mainly attributed to the OR under below-bandgap excitation [25]. However, the physical process is complicated under above-bandgap excitation as other optical effects would participate in the THz radiation, such as photogalvanic effect sensitive to the azimuthal angle and SDF insensitive to the azimuthal angle [26]. In Fig. 2(c), the isotropic response of the THz peak-valley amplitude dependence on the azimuthal angle suggests that the SDF dominates the THz radiation [27]. To our understanding, the thermal effect generally dominates for THz radiation in thermoelectric materials, such as Bi_2Te_3-based compounds [28] and layered cobaltite Ca_xCoO_2 [29], while the ZnSe crystal does not belong to the category of thermoelectric materials. Besides, the thermal effect depends on the generation of transient thermal gradients, which can be created by the thickness gradient of the sample and further generate thermoelectric current through the Seebeck effect [30]. However, the surface of the ZnSe crystal is uniformly flat without any thickness gradient, which can hardly form temperature gradient. Hence, the thermal effect has a negligible contribution to the THz radiation in the ZnSe crystal. The photo-Dember field-induced surface voltage is described by

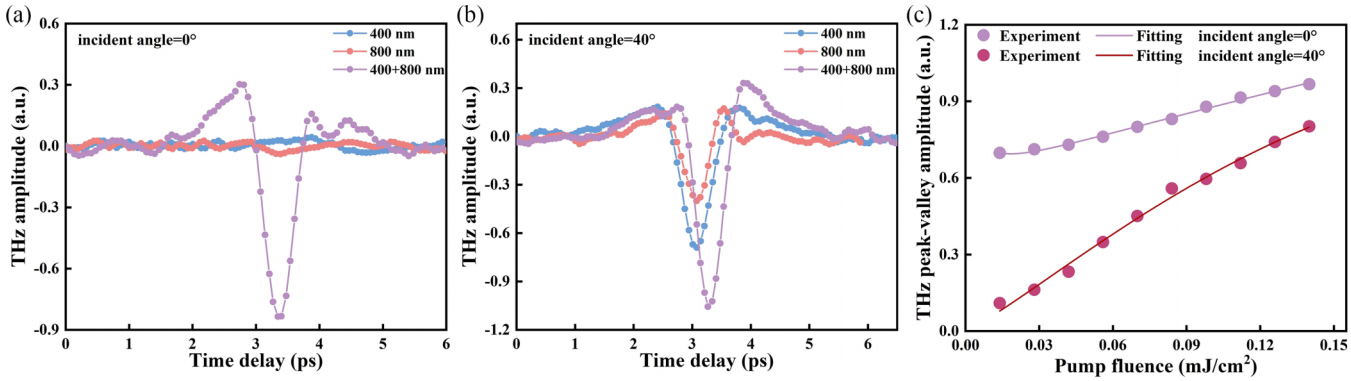

FIG. 3. THz time-domain signals of ZnSe with a fixed azimuthal angle at 0° under single 400-nm (blue), single 800-nm (red), and 400+800-nm (purple) excitations at (a) normal and (b) oblique incidences. (c) Pump fluence dependence of the THz peak-valley amplitude under the 400+800-nm excitation (normal incidence: purple; and oblique incidence: rose red). The dots are experimental results and the solid lines are fitting results.

the following equation: $V_D = \frac{k_B T}{e}\frac{b-1}{b+1}\ln(1+\frac{(b+1)\Delta n}{n_0 b+p_0})$, where $b = \mu_e/\mu_h$ is the mobility ratio of the electrons (μ_e) to holes (μ_h); n_0 and p_0 are the initial density of the electrons and holes [31], respectively. As such, the photo-Dember field generally dominates the THz emission in narrow-bandgap semiconductors with a large b. For example, the photo-Dember field is the primary mechanism for the THz radiation in InAs with $b \approx 125$ and InSb with $b \approx 95$ [31]. However, the carrier mobilities of the electrons and holes in ZnSe crystal are $260\,\mathrm{cm}^2/\mathrm{Vs}$ [32] and $26.8\,\mathrm{cm}^2/\mathrm{Vs}$ [21], respectively, which induce a much smaller b. Hence, the photo-Dember effect is not the dominant THz emission mechanism in ZnSe.

To further determine the THz radiation physical mechanism of ZnSe under single 800- and 400-nm excitations, we investigate the dependence of THz peak-valley amplitude on the pump fluence as presented in Fig. 2(d). Under single 400-nm (from 0.028 to 0.140 mJ/cm²) and 800-nm (from 0.07 to 0.35 mJ/cm²) excitations, the THz peak-valley amplitude remains a positive value as the pump fluence increases. It indicates that the polarity of the THz waveforms does not reverse with the increasing pump fluence. With the pump fluence increasing, the THz peak-valley amplitude demonstrates linear increase under single 800-nm excitation (red dots), while the THz peak-valley amplitude exhibits saturation under single 400-nm excitation (blue dots). The linear dependence with the pump fluence can be fitted well by a linear function, which is a feature of a second-order nonlinear optical effect as the THz electric field (E_{THz}) is quadratically proportional to the incident laser field (E_{in}) [16] as

$$E_{\mathrm{THz}} \propto \chi^{(2)} E_{in} E_{in}, \tag{2}$$

where $\chi^{(2)}$ represents the second-order nonlinear susceptibility. This further confirms that the OR dominates the THz radiation in the pump fluence region from 0.07 to 0.35 mJ/cm² under single 800-nm excitation [25]. On the contrary, the pump fluence dependence of THz radiation under single 400-nm excitation can be well fitted by [33,34]:

$$E_{\mathrm{THz}} \propto D I_{2\omega}/(I_{2\omega} + I_{\mathrm{sat}}), \tag{3}$$

where D is the scaling factor; the $I_{2\omega}$ and I_{sat} are the pump fluence and saturation pump fluence of 400-nm excitation, respectively. The saturation occurs due to the accumulation of photoexcited carriers on the surface under high excitation, resulting in the electrostatic shielding of SDF [27,35]. This result further suggests that the SDF dominates the THz radiation under single 400-nm excitation.

To suppress the effects of OR and SDF, the azimuthal angle of ZnSe is fixed at 0° (Fig. 2), where their contributions are minimal, while the quantum interference under 400+800-nm light excitation would take the dominant position. In this scenario, the THz generation resulting from the third-order nonlinear optical effect under two-color excitation can be ready to be detected. The pump fluences of the 400-nm, 800-nm, and 400+800-nm pulses are $0.014\,\mathrm{mJ/cm}^2$, $0.127\,\mathrm{mJ/cm}^2$, and $0.141\,\mathrm{mJ/cm}^2$, respectively. Their corresponding peak power densities are $4.0\times10^{12}\,\mathrm{W/m}^2$, $3.6\times10^{13}\,\mathrm{W/m}^2$, and $4.0\times10^{13}\,\mathrm{W/m}^2$. Figure 3(a) displays the THz time-domain waveforms under 400-nm (blue), 800-nm (red), and 400+800-nm (purple) pump pulse excitations under the same experimental condition at normal incidence. It is evident that the THz time-domain signal under 400+800-nm excitation is quite larger than those under single 800-nm and 400-nm excitations. Similarly, when the incident angle is 40°, the THz time-domain signal under 400+800-nm ($0.141\,\mathrm{mJ/cm}^2$) excitation is also larger than those under single 800-nm ($0.127\,\mathrm{mJ/cm}^2$) and 400-nm ($0.014\,\mathrm{mJ/cm}^2$) excitations as shown in Fig. 3(b). Compared with the 800-nm excitation, a β-BBO crystal and a filter have been added into the 400-nm excitation path, and a β-BBO crystal has been added into the 400+800-nm excitation path, as shown in Figs. 1(a) and 6 (Appendix A). In fact, the time delay between the 800-nm and 400+800-nm pulses is induced by the β-BBO crystal and the time delay between the 400-nm and 400+800-nm pulses is induced by the filter. To make a clear comparison of the time-domain signals between the 400-nm and 800-nm pulses, we have subtracted the long time delay induced by the filter and β-BBO crystal at the 400-nm excitation during the data processing. Hence, the time delay of the THz emission signal between the 400+800-nm and the 800-nm excitations is caused by the β-BBO crystal. Figure 8 (Appendix C) shows the corresponding frequency-domain THz spectra of the ZnSe crystal under the same excitation conditions. The bandwidths of THz spectra are 1.0, 1.2, and 1.3 THz under 400-nm

(blue), 800-nm (red), and 400+800-nm (purple) excitations, respectively. The broader THz bandwidth under 400+800-nm excitation is ascribed to more frequency mixing combinations compared to that of the single-color excitation [11].

Usually, the second-order nonlinear optical effect such as OR under the single-color excitation is hardly observed in centrosymmetric materials and only the single FWM mechanism is revealed for the THz radiation under normal-incident excitations such as Bi_2Se_3 [15], Bi_2S_3 [7], ITO films [9], and so forth. However, the competition between the OR, SDF, and FWM effect would emerge under oblique incidence, which would be difficult to be distinguished. To further verify the contributions of OR, SDF, and FWM effects to the THz generation under the 400+800-nm excitation, we investigate the dependence of the THz peak-valley amplitude on the pump fluence (from 0.014 to 0.140 mJ/cm²) under both normal and oblique incidences as shown in Fig. 3(c). Under the 400+800-nm excitation, the THz peak-valley amplitude remains positive value as the pump fluence increases, indicating that the THz waveform polarity does not reverse with the increasing pump fluence. When the pure FWM effect dominates THz generation, the THz peak-valley amplitude shows a high-order dependence on the pump fluence [9,11]. However, in our experiment, the THz peak-valley amplitude displays a saturation dependence with the pump fluence under two-color oblique incidence, suggesting the activation of other optical effects to compete with the FWM effect. According to the net FWM model, the THz amplitude can be described by [14,36]

$$E_{\mathrm{THz}} \propto \partial j/\partial t = 2\chi^{(3)} E_\omega^* E_\omega^* E_{2\omega} \sin(\Delta\varphi), \tag{4}$$

where E_ω and $E_{2\omega}$ represent the electric field of the ω and 2ω; the $\chi^{(3)}$ represents the third-order nonlinear susceptibility; $\Delta\varphi$ is the relative phase difference between the ω and 2ω waves. Considering the OR, SDF, and FWM to the THz generation in ZnSe crystal, the THz electric field can be simplified as follows (details in Appendix E):

$$E_{\mathrm{THz}} \propto aI + bI^{3/2} + fI/(gI + I_{\mathrm{sat}}), \tag{5}$$

where the a, b, f, and g are related to the constants and nonlinear susceptibility. The three items from left to right represent the contributions of OR, FWM, and the SDF to THz radiation, respectively. After fitting with Eq. (5), the contribution ratio of the OR to FWM is approximate 1:2 under normal incidence, while the contribution ratios among the OR, FWM, and SDF are approximate 1.7:1:4.2 under oblique incidence. These fitting results demonstrate that the FWM dominates THz generation of ZnSe under normal incidence, while the SDF dominates THz generation of ZnSe under oblique incidence. Furthermore, we have demonstrated experimentally and theoretically that in the FWM model, the THz amplitude has a quadratic dependence on the fluence of the 800-nm laser (see detailed calculation in Appendix E).

In order to complementarily confirm the interplay between the OR, SDF, and FWM effects to THz generation in ZnSe, we have investigated the dependence of the THz amplitude on the relative phase difference between ω (800-nm) and 2ω (400-nm) waves at normal incidence and oblique incidence as displayed in Figs. 4(a) and 4(b), respectively. As a comparison, the THz amplitude shows a slight positive shift from the zero axis at normal incidence, while the THz amplitude exhibits a significant shift away from the zero axis at oblique incidence, as indicated by the purple arrows. Under the two-color excitation, when the THz generation is attributed to pure FWM effect [(Eq. (4)], the dependence of the THz peak-valley amplitude on the relative phase difference should exhibit a sine symmetry distribution with the zero axis as seen in Bi_2Se_3 [15], Bi_2S_3 [7], and ITO films [9]. However, if other optical effects are activated, the sine symmetry with the zero axis would be broken, as previously observed in InAs [8] and ZnTe [10]. In this scenario, the dependence of the THz peak-valley amplitude on the relative phase difference $\Delta\varphi$ can be described as follows:

$$E_{\mathrm{THz}} \propto 2\chi^{(3)} E_\omega^* E_\omega^* E_{2\omega} \sin(\Delta\varphi) + G, \tag{6}$$

where the G is a constant related to other optical effects and it is insensitive to the relative phase difference between ω and 2ω waves. The results can be fitted well by Eq. (6), as shown in Figs. 4(a) and 4(b). Hence, the THz signal shifts observed at normal incidence is ascribed to OR, while that at oblique incidence originates from the combined effects of OR and SDF. Both THz amplitude shifts are insensitive to the relative phase difference between ω (800-nm) and 2ω (400-nm) waves. In order to portray the THz generation from each origin individually, we define the C_{OR}, C_{FWM}, and C_{SDF} to represent the THz time-domain peak-valley amplitude that are induced by the OR, FWM, and SDF, respectively. We first extract the THz time-domain waveforms at relative phase differences of $\pi/2$ (red line) and $3\pi/2$ (blue line) under normal [Fig. 4(c)] and oblique incidences [Fig. 4(d)]. According to Eq. (6), FWM and OR provide a constructive contribution to the THz generation at a phase difference of $\pi/2$ and a destructive effect of $3\pi/2$ with the reversal polarity of THz time-domain waveforms. Therefore, the THz time-domain waveforms with the relative phase difference at $\pi/2$ and $3\pi/2$ under normal incidence [Fig. 4(c)] can be described as: $C_{\mathrm{OR}} + C_{\mathrm{FWM}}$ and $C_{\mathrm{OR}} - C_{\mathrm{FWM}}$, respectively. The contribution of the THz generation that comes from the OR (purple line) can be obtained by calculating the $((C_{\mathrm{OR}} - C_{\mathrm{FWM}}) + (C_{\mathrm{OR}} + C_{\mathrm{FWM}}))/2$. The contribution of the net FWM (orange line) to THz generation can be obtained by calculating the $((C_{\mathrm{OR}} + C_{\mathrm{FWM}}) - (C_{\mathrm{OR}} - C_{\mathrm{FWM}}))/2$. The calculated result in Fig. 4(c) shows the contribution ratio between the OR and FWM is approximate 1:2.3. Similarly, under the oblique incidence [Fig. 4(d)], the THz time-domain waveforms with relative phase difference at $\pi/2$ and $3\pi/2$ are described as: $C_{\mathrm{OR}} + C_{\mathrm{SDF}} + C_{\mathrm{FWM}}$ and $C_{\mathrm{OR}} + C_{\mathrm{SDF}} - C_{\mathrm{FWM}}$. We directly extract the THz radiation from net FWM contribution with $\Delta\varphi = \pi/2$ by $((C_{\mathrm{OR}} + C_{\mathrm{SDF}} + C_{\mathrm{FWM}}) - (C_{\mathrm{OR}} + C_{\mathrm{SDF}} - C_{\mathrm{FWM}}))/2$, while that with $\Delta\varphi = 3\pi/2$ is calculated by $((C_{\mathrm{OR}} + C_{\mathrm{SDF}} - C_{\mathrm{FWM}}) - (C_{\mathrm{OR}} + C_{\mathrm{SDF}} + C_{\mathrm{FWM}}))/2$. Based on the contribution of the OR under normal incidence, the contribution of the OR under the oblique incidence can be calculated [the purple line in Fig. 4(d)] by $E_{THz-OR}^{\mathrm{oblique}} \approx E_{THz-OR}^{\mathrm{normal}}/\cos 40^\circ$ [24], where the $E_{THz-OR}^{\mathrm{oblique}}$ and $E_{THz-OR}^{\mathrm{normal}}$ are THz radiation due to the OR under oblique and normal incidences, respectively. Finally, the contribution of the SDF (green line) to the THz radiation can be obtained by $((C_{\mathrm{OR}} + C_{\mathrm{SDF}} + C_{\mathrm{FWM}}) - (C_{\mathrm{Net\,OR}} + C_{\mathrm{Net\,FWM}}))$. After the calculation, the result shows the contribution ratios among the OR, FWM, and

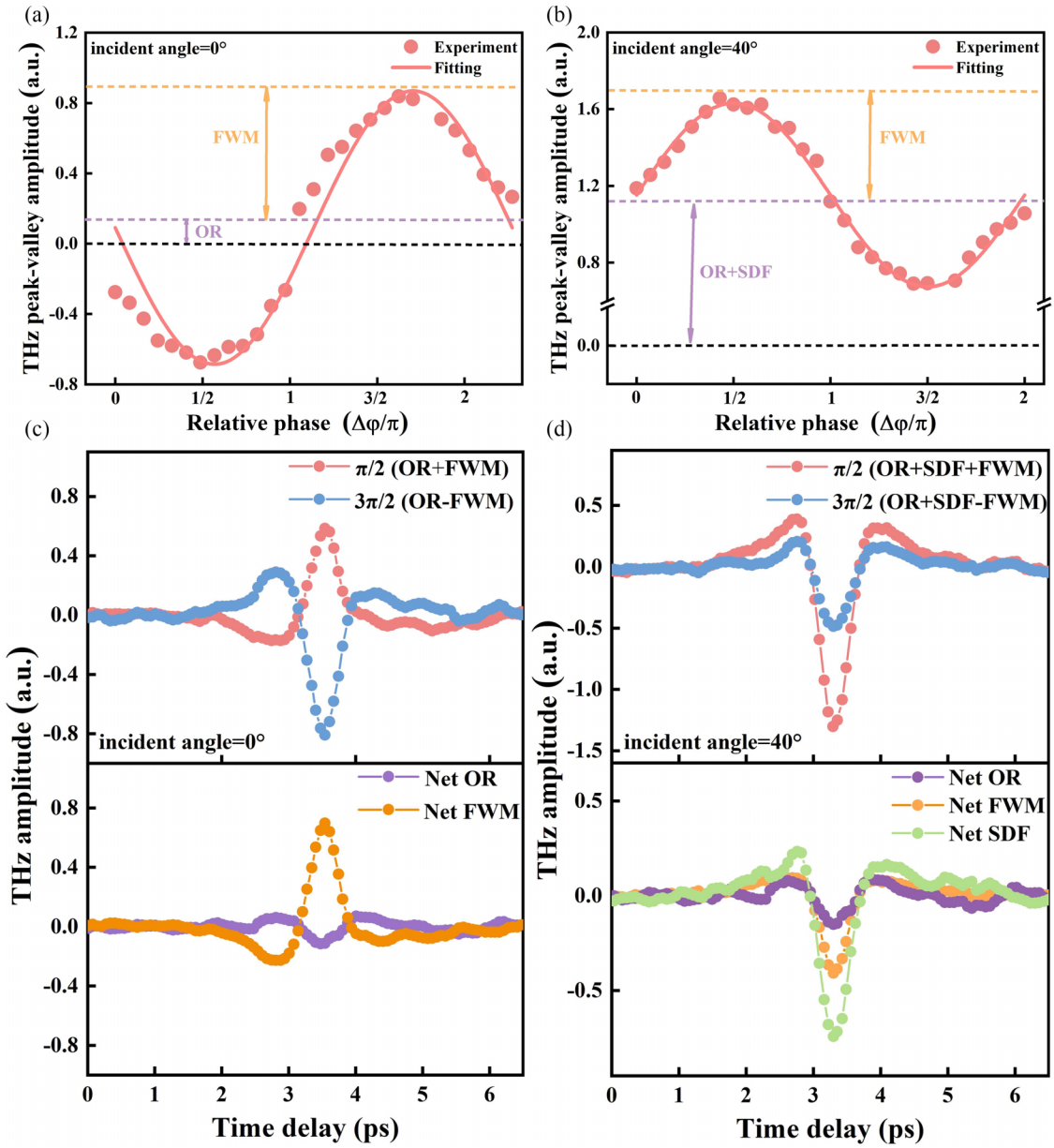

FIG. 4. THz peak-valley amplitude with the relative phase difference between ω (800-nm) and 2ω (400-nm) light at (a) normal and (b) oblique incidences. The dots and lines present the experimental and fitting results, respectively. (c), (d) The red and blue lines represent the THz time-domain signals with the relative phase difference at $\pi/2$ and $3\pi/2$ (upper). The purple, orange, and green lines represent the THz generation from the net OR, FWM, and SDF effects, respectively (bottom).

SDF are approximate 1.5:1:6.7. These experimental results are in agreement with the pump fluence-dependent fitting results. In addition, after removing the net OR and SDF contributions, we have investigated the dependence of the net FWM on relative phase difference. As shown in Fig. 5, we observe the THz time-domain signal with a polarity reversal and almost the same amplitude at the phase differences of $\pi/2$ and $3\pi/2$, no matter the ZnSe is excited under normal [Fig. 5(a)] or oblique incidence [Fig. 5(b)]. This time-domain THz waveform polarity reversal with $\Delta\varphi$ is the feature of quantum interference in momentum space due to the simultaneous one-photon and two-photon absorptions [4]. This result also indicates that quantum interference can be veiled by other multiple optical effects, which need to be handled with patience. Furthermore, we have also obtained the THz electric field as 1.92×10^4 V/m, and the THz emission efficiency per length is approximately 2.7×10^6 V/J under the 400+800-nm excitation at the fixed pump fluence of 0.140 mJ/cm^2 (see detailed calculation in Appendix F).

III. CONCLUSION

In summary, we have studied the photophysics mechanism of the THz radiation from ZnSe crystal under single 800-nm (ω), single 400-nm (2ω), and 400+800-nm laser excitations, which are ascribed to the OR, SDF, and FWM effects. Their net contributions to the THz radiation can be distinguished by the characterization of the azimuthal angle dependence, pump

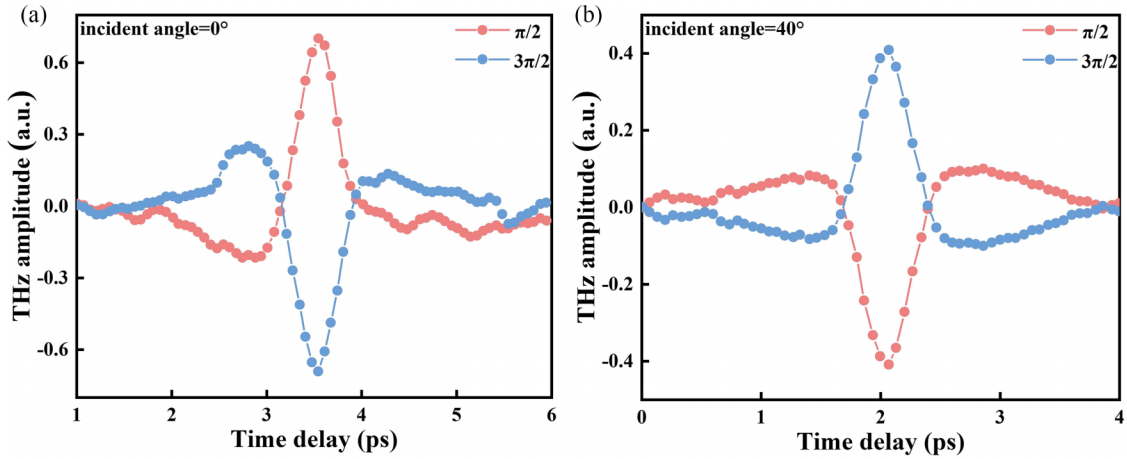

FIG. 5. THz time-domain waveforms originating from net FWM when the phase difference between the ω (800-nm) and 2ω (400-nm) waves is $\pi/2$ (red) and $3\pi/2$ (blue) under (a) normal incidence and (b) oblique incidence of the pump beam.

fluence dependence, and relative phase difference between the ω and 2ω waves under both normal and oblique incidences. The quantum interference with the signal feature of a polarity reversal at the phase differences of $\pi/2$ and $3\pi/2$ is clearly observed under both normal and oblique incidences. This work not only elucidates the THz radiation properties of ZnSe crystal but also affords a tool to distinguish different optical effects in semiconductors for coherent control of ultrafast photocurrents by THz emission spectroscopy.

ACKNOWLEDGMENTS

This work was supported by the National Natural Science Foundation of China (Grants No. 12261141662, No. 12074311, and No. 12374315).

APPENDIX A: EXPERIMENTAL SETUP OF SINGLE-COLOR LASER EXCITATION

Figures 6(a) and 6(b) are the schematic diagram of single 800-nm and single 400-nm laser excitation, respectively. Compared to the experimental setup at 800-nm excitation, the 400-nm laser pulse is produced by the frequency-doubling process of the 800-nm laser pulse after passing through a β-BBO crystal and the residual 800-nm pulse is filtered out through a short-pass filter as shown in Fig. 6(b).

APPENDIX B: RAMAN SPECTRUM OF ZnSe CRYSTAL

The p-type of ZnSe crystal with an orientation of ⟨001⟩ and a flat polished surface is commercially provided by Heifei Kejing Materials Technology Company. Figure 7 displays the Raman spectrum of the ZnSe crystal (0.5 mm) excited with a 532-nm laser. The SmartRaman confocal micro-Raman module, developed by the Institute of Semiconductors, Chinese Academy of Sciences, was used for the Raman measurement. The optical image of ZnSe crystal is presented in the inset of Fig. 7. Two characteristic peaks are observed at 201 and 248 cm^{-1}, corresponding to the transverse optical and longitudinal optical phonon modes [37–39]. Raman spectroscopy is used to characterize whether the ZnSe crystal is oxidized. Our measurements indicate that the Raman spectrum of ZnSe crystal does not contain oxidation peaks [40].

APPENDIX C: FREQUENCY-DOMAIN SIGNALS OF ZnSe AT OBLIQUE INCIDENCE

Figure 8 shows the corresponding frequency-domain THz spectra of the ZnSe crystal after the Fourier transformation. The bandwidths of THz spectra are 1.0, 1.2, and 1.3 THz under single 400-nm (blue), single 800-nm (red), and 400+800-nm (purple) excitations, respectively.

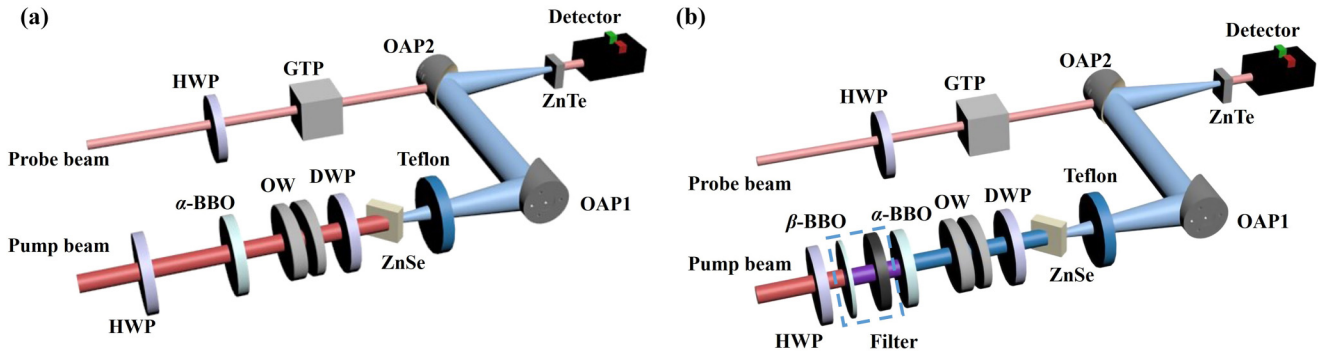

FIG. 6. Schematic diagram of (a) single 800-nm and (b) single 400-nm laser excitations.

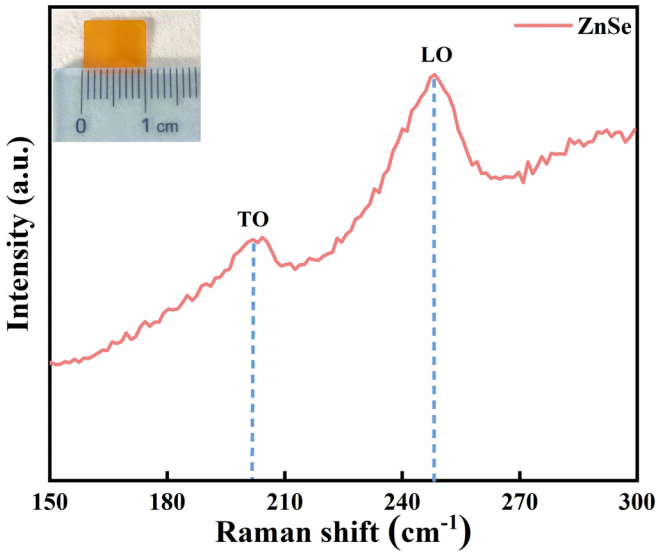

FIG. 7. Raman spectrum of ZnSe crystal excited with a 532-nm laser. Inset: optical image of ZnSe crystal.

APPENDIX D: THz RADIATION DEPENDENCE ON ZnSe CRYSTAL AZIMUTHAL ANGLE

The THz electric field induced by the OR effect is described as: $E_{\mathrm{THz}} \propto \partial^2 P/\partial t^2$ [24]. The nonlinear polarization P is described as follows: $P_i^{(2)}(\Omega) = \sum_{j,k} \varepsilon_0 \chi_{ijk}^{(2)\mathrm{eff}}(\Omega, \omega+\Omega, -\omega) E_j(\omega+\Omega) E_k^*(\omega)$ [16], where the $\chi_{ijk}^{(2)\mathrm{eff}}$ is the effective second-order nonlinear susceptibility tensor; ω is fundamental frequency, and Ω is the THz radiation frequency. According to the $\bar{4}3m$ point group of ZnSe, the nonzero elements of the second-order nonlinear susceptibilities $\chi_{ijk}^{(2)\mathrm{eff}}$ are shown as follows:

$$d_{il} = \frac{1}{2}\chi_{ijk}^{(2)\mathrm{eff}} \begin{bmatrix} 0 & 0 & 0 & d_{14} & 0 & 0 \\ 0 & 0 & 0 & 0 & d_{25} & 0 \\ 0 & 0 & 0 & 0 & 0 & d_{36} \end{bmatrix}. \tag{D1}$$

The establishment of the laboratory coordinate system and the crystalline coordinate system is the same as that in Ref. [41]. The electric field can be obtained by rotating the plane of $X'Y'$ along the Z' axis for γ (the azimuthal angle of the ZnSe crystal):

$$\begin{aligned} \begin{bmatrix} E_X \\ E_Y \\ E_Z \end{bmatrix} &= \begin{bmatrix} \cos\gamma & \sin\gamma & 0 \\ -\sin\gamma & \cos\gamma & 0 \\ 0 & 0 & 1 \end{bmatrix} \begin{bmatrix} E_x \\ E_y \\ E_z \end{bmatrix} \\ &= \begin{bmatrix} \cos\gamma & \sin\gamma & 0 \\ -\sin\gamma & \cos\gamma & 0 \\ 0 & 0 & 1 \end{bmatrix} \begin{bmatrix} -E_0\cos\psi\cos\theta \\ E_0\sin\psi \\ E_0\cos\psi\sin\theta \end{bmatrix} \\ &= \begin{bmatrix} -E_0\cos\psi\cos\theta\cos\gamma + E_0\sin\psi\sin\gamma \\ E_0\cos\psi\cos\theta\sin\gamma + E_0\sin\psi\cos\gamma \\ E_0\cos\psi\sin\theta \end{bmatrix}, \end{aligned} \tag{D2}$$

where the ψ and θ are the polarization angle and incident angle of the pump laser, respectively. Herein, we fix the $\psi = 0^\circ$ and the $\theta = 40^\circ$ (0°) to investigate the azimuthal angle dependence. Then the nonlinear polarization is obtained as follows:

$$\begin{aligned} P = \begin{bmatrix} P_X \\ P_Y \\ P_Z \end{bmatrix} &= 2\varepsilon_0 \begin{bmatrix} 0 & 0 & 0 & d_{14} & 0 & 0 \\ 0 & 0 & 0 & 0 & d_{25} & 0 \\ 0 & 0 & 0 & 0 & 0 & d_{36} \end{bmatrix} \begin{bmatrix} E_X^2 \\ E_Y^2 \\ E_Z^2 \\ 2E_Y E_Z \\ 2E_Z E_X \\ 2E_X E_Y \end{bmatrix} \\ &= \varepsilon_0 \begin{bmatrix} d_{14}\sin 2\gamma \\ 2d_{25}\sin\gamma \\ 2d_{36}\cos\gamma \end{bmatrix}. \end{aligned} \tag{D3}$$

Hence, the THz electric field can be obtained as follows:

$$E_{\mathrm{THz}} \propto A\sin 2\gamma + B\sin(\gamma + \pi/4) + C. \tag{D4}$$

The A and B are the constants related to the nonlinear susceptibility, while the C is a constant independent on the nonlinear susceptibility. The blue dots in Fig. 2(b) are well fitted by using Eq. (D4).

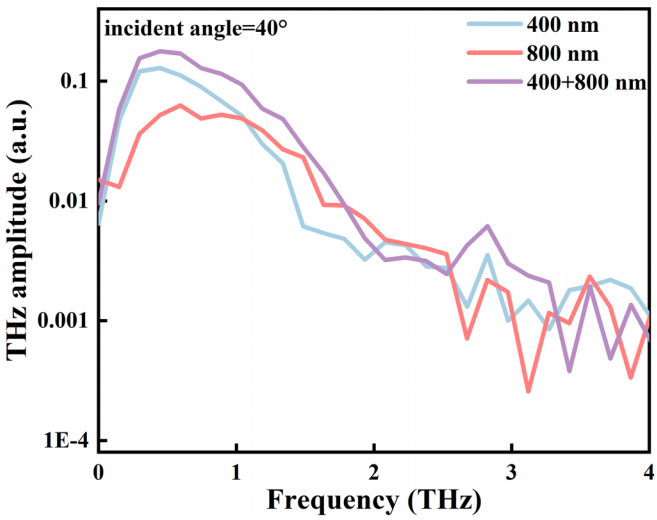

FIG. 8. Frequency-domain signals of ZnSe under single 400-nm (blue), single 800-nm (red), and 400+800-nm (purple) excitations at 40° oblique incidence.

APPENDIX E: THz PEAK-VALLEY AMPLITUDE DEPENDENCE ON THE PUMP FLUENCE UNDER 400+800-nm EXCITATION

According to the net FWM model, the THz amplitude is described by [14,36]

$$E_{\mathrm{THz}} \propto \partial j/\partial t = 2\chi^{(3)} E_\omega^* E_\omega^* E_{2\omega} \sin(\Delta\varphi), \tag{E1}$$

where the E_ω and $E_{2\omega}$ represent the electric field of the ω and 2ω; the $\chi^{(3)}$ represents the third-order nonlinear susceptibility; $\Delta\varphi$ is the relative phase difference between the ω and 2ω waves. Since the $I_\omega \propto E_\omega^2$ and $I_{2\omega} \propto E_{2\omega}^2$, the THz electric field originating from net FWM is described as: $E_{\mathrm{THz}} \propto I_\omega I_{2\omega}^{1/2}$.

Based on the experimental situation, the I is the total pump fluence before the β-BBO; α is the conversion efficiency of the β-BBO. Hence, the electric field of the ω and 2ω are described as follows: (1-α) I and αI, respectively. Based on the above discussions, the pump fluence (1-α) I would be divided into two parts: one part is used to participate in the process of OR, denoted (1-α) ηI, and the remaining part is used to participate in FWM, denoted as (1-α) (1-η) I. Similarly, the αI would be divided into two parts: one part is used to participate in the process of SDF, denoted $\alpha\xi I$, and the remaining part is used to participate in FWM, denoted as α(1-ξ) I. The η and ξ are scaling factors. Considering the contributions of OR, SDF, and FWM to THz generation of ZnSe crystal, the generated THz electric field of ZnSe crystal can be described as follows:

$$E_{\mathrm{THz}} \propto \chi^{(2)}(1-\alpha)\eta I + \chi^{(3)}(1-\alpha)(1-\eta)I(1-\xi)\alpha I^{1/2} + F\alpha\xi I/(\alpha\xi I + I_{\mathrm{sat}}), \tag{E2}$$

where F is scaling factor and I_{sat} is the saturation pump fluence of 400-nm light due to the accumulation of photoexcited carriers on the surface under high excitation. Then the THz electric field is simplified as

$$E_{\mathrm{THz}} \propto aI + bI^{3/2} + fI/(gI + I_{\mathrm{sat}}), \tag{E3}$$

where the a, b, f, and g are related to the constants and nonlinear susceptibility terms as

$$\begin{aligned} a &= \chi^{(2)}(1-\alpha)\eta, \\ b &= \chi^{(3)}(1-\alpha)(1-\eta)(1-\xi)\alpha, \\ f &= F\alpha\xi, \\ g &= \alpha\xi. \end{aligned} \tag{E4}$$

In our experiment, the 2ω light is generated via a second harmonic generation process when the ω light passes through the β-BBO crystal. Then the electric field of the 2ω can be described by $E_{2\omega} \propto \chi^{(2)}E_\omega E_\omega$. Therefore, in the FWM model, the THz amplitude with respect to the ω light can be described by $E_{\mathrm{THz}} \propto 2\chi^{(3)}\chi^{(2)}E_\omega^* E_\omega^* E_\omega E_\omega \sin(\Delta\varphi)$, suggesting a quadratic dependence of the THz signal on the pump fluence I of the ω light. In order to confirm this deduction, we have measured the THz peak-valley amplitude with respect to the increasing pump fluence of the 800-nm light, as shown in Fig. 9. It is evident that the THz amplitude presents quadratic dependences under both normal- and oblique-incident excitations, which can be fitted well by quadratic functions.

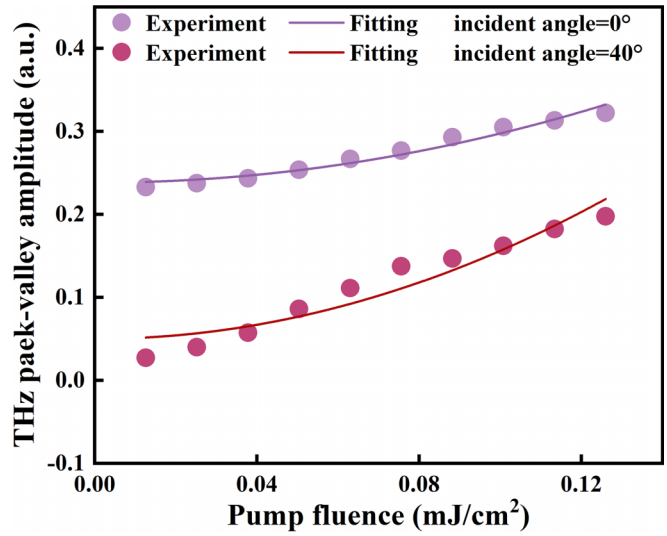

FIG. 9. Pump fluence dependence of the THz peak-valley amplitude under 800-nm excitation in FWM model (normal incidence: purple; oblique incidence: rose red). The dots and solid lines represent experimental and fitting results, respectively.

APPENDIX F: THE THz ELECTRIC FIELD AND THz EMISSION EFFICIENCY OF ZnSe

The thickness of the ZnSe crystal is 0.5 mm, which is supplied by the Heifei Kejing Materials Technology Company. The THz time-domain signal is detected by the electro-optical sampling technique. Thus, we use the absolute value of the THz electric field to characterize the optical-to-THz conversion efficiency as follows [42]:

$$\frac{\Delta I}{I_{\mathrm{probe}}} = \frac{\omega n^3 E_{\mathrm{THz}} r_{41} L}{c}, \tag{F1}$$

where the nonzero electro-optic coefficient (ZnTe) $r_{41} = 3.9\,\mathrm{pm/V}$; the refractive index of the ZnTe detection crystal at 800 nm is $n = 2.8$ and its length is $L = 2$ mm; c and ω are the speed of light and the circular frequency of the probe light. In the experiment, I_{probe} is 0.6 μA, and the measured electric signal from the Lock-in amplifier is $\Delta I = 0.16\,\mathrm{nA}$. Therefore, we can calculate the peak value of the THz electric field from ZnSe crystal as $E_{\mathrm{THz}} = 1.92 \times 10^4\,\mathrm{V/m}$ under the 400+800-nm excitation. Then the THz emission efficiency (£) per length can be calculated as [43]

$$£ = |E_{\mathrm{THz}}|/F_{\mathrm{pump}}d = 2.7 \times 10^6\,\mathrm{V/J}, \tag{F2}$$

where F_{pump} is the pump fluence ($0.140\,\mathrm{mJ/cm^2}$) and d is the thickness of the ZnSe crystal.

[1] C. Chen, Y. Y. Yin, and D. S. Elliott, Interference between optical transitions, Phys. Rev. Lett. **64**, 507 (1990).
[2] J. L. Krause, M. Shapiro, and P. Brumer, Coherent control of bimolecular chemical reactions, J. Chem. Phys. **92**, 1126 (1990).
[3] E. Dupont, P. B. Corkum, H. C. Liu, M. Buchanan, and Z. R. Wasilewski, Phase-controlled currents in semiconductors, Phys. Rev. Lett. **74**, 3596 (1995).
[4] A. Haché, Y. Kostoulas, R. Atanasov, J. L. P. Hughes, J. E. Sipe, and H. M. van Driel, Observation of coherently controlled photocurrent in unbiased, bulk GaAs, Phys. Rev. Lett. **78**, 306 (1997).
[5] M. J. Stevens, A. L. Smirl, R. D. R. Bhat, J. E. Sipe, and H. M. van Driel, Coherent control of an optically injected ballistic spin-polarized current in bulk GaAs, J. Appl. Phys. **91**, 4382 (2002).

[6] Z. Lü, D. Zhang, Z. Zhou, L. Sun, Z. Zhao, and J. Yuan, Coherently controlled terahertz source for a time domain spectroscopy system via injection current in bulk ZnSe, Appl. Opt. **51**, 676 (2012).

[7] Y. He, Y. Chen, C. Lu, Y. Zhang, Z. Tian, X. Xu, and J. Dai, Coherent injection photocurrent in bismuth sulfide film induced by one-plus-two photon absorption quantum interference, Opt. Lett. **47**, 1206 (2022).

[8] J. S. Totero Gongora, L. Peters, J. Tunesi, V. Cecconi, M. Clerici, A. Pasquazi, and M. Peccianti, All-optical two-color terahertz emission from quasi-2D nonlinear surfaces, Phys. Rev. Lett. **125**, 263901 (2020).

[9] Y. He, Y. Chen, J. Zhao, Z. Tian, and J. Dai, Coherent terahertz radiation from indium tin oxide film via third-order optical nonlinearity, Appl. Phys. Lett. **122**, 041106 (2023).

[10] L. Peters, J. S. Totero Gongora, V. Cecconi, L. Olivieri, J. Tunesi, A. Pasquazi, and M. Peccianti, Concurrent terahertz generation via quantum interference in a quadratic media, Adv. Opt. Mater. **11**, 2202578 (2023).

[11] Y. Lu, X. Zhang, Q. Xu, W. Jia, X. Feng, X. Chen, Y. Gu, Y. Yang, W. Zhang, and J. Han, Two-color-driven controllable terahertz generation in ITO thin film, ACS Photonics **11**, 293 (2024).

[12] L. Costa, M. Betz, M. Spasenovic, A. D. Bristow, and H. M. Van Driel, All-optical injection of ballistic electrical currents in unbiased silicon, Nat. Phys. **3**, 632 (2007).

[13] X. Y. Yu, Q. Luo, W. L. Li, Q. Li, Z. R. Qiu, and J. Y. Zhou, Ultrafast phase dynamics of coherent carriers in GaAs, Appl. Phys. Lett. **73**, 3321 (1998).

[14] D. Sun, C. Divin, J. Rioux, J. E. Sipe, C. Berger, W. A. de Heer, P. N. First, and T. B. Norris, Coherent control of ballistic photocurrents in multilayer epitaxial graphene using quantum interference, Nano Lett. **10**, 1293 (2010).

[15] D. A. Bas, K. Vargas-Velez, S. Babakiray, T. A. Johnson, P. Borisov, T. D. Stanescu, D. Lederman, and A. D. Bristow, Coherent control of injection currents in high-quality films of Bi_2Se_3, Appl. Phys. Lett. **106**, 041109 (2015).

[16] Y. Huang, L. Zhu, Q. Zhao, Y. Guo, Z. Ren, J. Bai, and X. Xu, Surface optical rectification from layered MoS_2 crystal by THz time-domain surface emission spectroscopy, ACS Appl. Mater. Interfaces **9**, 4956 (2017).

[17] X. Cao, Y. Huang, Y. Xi, Z. Lei, W. Du, T. Han, J. Wang, H. Wang, J. Chang, L. Zhu, Y. Zhou, S. Zhang, and X. Xu, Interplay between ultrafast shift current and ultrafast photon drag current in tellurium nanotubes, ACS Photonics **9**, 3144 (2022).

[18] J. N. Heyman, N. Coates, A. Reinhardt, and G. Strasser, Diffusion and drift in terahertz emission at GaAs surfaces, Appl. Phys. Lett. **83**, 5476 (2003).

[19] R. W. Boyd, A. L. Gaeta, and E. Giese, Nonlinear optics, *Springer Handbook of Atomic, Molecular, and Optical Physics* (Springer, Berlin, 2008), pp. 1097.

[20] D. N. Nikogosyan, *Nonlinear Optical Crystals: A Complete Survey* (Springer, New York, 2005).

[21] J. Ding, C. Liu, L. Xi, J. Xi, and J. Yang, Thermoelectric transport properties in chalcogenides ZnX (X = S, Se): From the role of electron-phonon couplings, J. Materiomics **7**, 310 (2021).

[22] B. Setera, C.-H. Su, B. Arnold, F.-S. Choa, L. Kelly, R. Sood, and N. B. Singh, Comparative study of bulk and nanoengineered doped ZnSe, Crystals **12**, 71 (2022).

[23] J. F. Holzman and A. Y. Elezzabi, Two-photon photoconductive terahertz generation in ZnSe, Appl. Phys. Lett. **83**, 2967 (2003).

[24] Z. Lei, Y. Huang, Z. Fan, W. Du, C. He, H. Wang, Y. Jin, and X. Xu, Terahertz emission from in-plane and out-of-plane dipoles in layered SnS_2 crystal, Appl. Phys. Lett. **116**, 161901 (2020).

[25] X. Wu, X. Chen, F. Zhao, T. Jia, and G. Wang, Terahertz radiation mechanisms in ZnSe at femtosecond laser pulse excitation, Jpn. J. Appl. Phys. **46**, 1497 (2007).

[26] Y. Huang, L. Zhu, Z. Yao, L. Zhang, C. He, Q. Zhao, J. Bai, and X. Xu, Terahertz surface emission from layered MoS_2 crystal: Competition between surface optical rectification and surface photocurrent surge, J. Phys. Chem. C **122**, 481 (2018).

[27] L. Zhang, Y. Huang, Q. Zhao, L. Zhu, Z. Yao, Y. Zhou, W. Du, and X. Xu, Terahertz surface emission of d-band electrons from a layered tungsten disulfide crystal by the surface field, Phys. Rev. B **96**, 155202 (2017).

[28] K. Takahashi, T. Kanno, A. Sakai, H. Tamaki, H. Kusada, and Y. Yamada, Terahertz radiation via ultrafast manipulation of thermoelectric conversion in thermoelectric thin films, Adv. Opt. Mater. **2**, 428 (2014).

[29] K. Takahashi, T. Kanno, A. Sakai, H. Tamaki, and Y. Yamada, Picosecond thermoelectric dynamics in layered cobaltite thin films probed by terahertz emission spectroscopy, Phys. Rev. B **92**, 094307 (2015).

[30] W. Lu, Z. Fan, Y. Yang, J. Ma, J. Lai, X. Song, X. Zhuo, Z. Xu, J. Liu, X. Hu, S. Zhou, F. Xiu, J. Cheng, and D. Sun, Ultrafast photothermoelectric effect in Dirac semimetallic Cd_3As_2 revealed by terahertz emission, Nat. Commun. **13**, 1623 (2022).

[31] P. Gu, M. Tani, S. Kono, K. Sakai, and X.-C. Zhang, Study of terahertz radiation from InAs and InSb, J. Appl. Phys. **91**, 5533 (2002).

[32] I. Kikuma, M. M. Masatoshi Matsuo, and T. K. Toyokazu Komuro, In situ annealing of melt-grown ZnSe crystals under Zn partial pressure, Jpn. J. Appl. Phys. **31**, L531 (1992).

[33] M. Reid and R. Fedosejevs, Terahertz emission from (100) InAs surfaces at high excitation fluences, Appl. Phys. Lett. **86**, 011906 (2004).

[34] Y. Xi, Y. Zhou, Z. Lei, X. Cao, J. Wang, Y. Ge, Y. Huang, L. Zhu, and X. Xu, Thickness-dependent terahertz emission from Bi_2S_3 films under excitation below and above the band gap, Phys. Rev. B **107**, 035307 (2023).

[35] J. F. Federici, B. Schulkin, F. Huang, D. Gary, R. Barat, F. Oliveira, and D. Zimdars, THz imaging and sensing for security applications—explosives, weapons and drugs, Semicond. Sci. Technol. **20**, S266 (2005).

[36] K. Y. Kim, J. H. Glownia, A. J. Taylor, and G. Rodriguez, Terahertz emission from ultrafast ionizing air in symmetry-broken laser fields, Opt. Express **15**, 4577 (2007).

[37] J. C. Irwin and J. LaCombe, Second-order Raman spectrum of ZnSe, Can. J. Phys. **48**, 2499 (1970).

[38] L. S. Basalaeva, V. P. Grafova, T. A. Duda, N. N. Kurus, R. B. Vasiliev, and A. G. Milekhin, Phonons of atomically thin ZnSe nanoplatelets grown by the colloidal method, J. Phys. Chem. C **127**, 13112 (2023).

[39] P. Gupta, R. G. Solanki, P. Patel, K. M. Sujata, R. Kumar, and A. Pandit, Enhanced antibacterial and photoluminescence activities of ZnSe nanostructures, ACS Omega **8**, 13670 (2023).

[40] R. L. d. S. Silvae and A. Franco, Jr., Raman spectroscopy study of structural disorder degree of ZnO ceramics, Mater. Sci. Semicond. Process. **119**, 105227 (2020).

[41] J. Wang, Y. Huang, Z. Lei, Y. Xi, W. Du, X. Cao, Y. Ge, L. Zhu, Y. Zhou, and X. Xu, Tunable polarized terahertz wave generation induced by spontaneous polarization-dependent ultrafast shift current from vertically grown ferroelectric SnS, Phys. Rev. B **106**, 235308 (2022).

[42] P. C. M. Planken, H.-K. Nienhuys, H. J. Bakker, and T. Wenckebach, Measurement and calculation of the orientation dependence of terahertz pulse detection in ZnTe, J. Opt. Soc. Am. B **18**, 313 (2001).

[43] J. Maysonnave, S. Huppert, F. Wang, S. Maero, C. Berger, W. de Heer, T. B. Norris, L. A. De Vaulchier, S. Dhillon, J. Tignon, R. Ferreira, and J. Mangeney, Terahertz generation by dynamical photon drag effect in graphene excited by femtosecond optical pulses, Nano Lett. **14**, 5797 (2014).